



1 **Representation of iron aerosol size distributions is critical in**  
2 **evaluating atmospheric soluble iron input to the ocean**

3 Mingxu Liu<sup>1,2</sup>, Hitoshi Matsui<sup>1</sup>, Douglas S. Hamilton<sup>3</sup>, Sagar D. Rathod<sup>4</sup>, Kara D. Lamb<sup>5</sup>, Natalie M.  
4 Mahowald<sup>6</sup>

5 <sup>1</sup>Graduate School of Environmental Studies, Nagoya University, Nagoya, Japan

6 <sup>2</sup>College of Environmental Science and Engineering, Peking University, Beijing, China

7 <sup>3</sup>Department of Marine, Earth, and Atmospheric Sciences, North Carolina State University, Raleigh, NC, USA

8 <sup>4</sup>La Follette School of Public Affairs, University of Wisconsin-Madison, Madison, WI, USA

9 <sup>5</sup>Department of Earth and Environmental Engineering, Columbia University, New York, NY, USA

10 <sup>6</sup>Department of Earth and Atmospheric Science, Cornell University, Ithaca, NY, USA

11 *Correspondence to:* H.M. (matsui@nagoya-u.jp)

12 **Abstract.** Atmospheric aerosol deposition acts as a major source of soluble (bioavailable) iron in open ocean regions where it  
13 limits phytoplankton growth and primary production. The aerosol size distribution of emitted iron particles, along with particle  
14 growth from mixing with other atmospheric components, is an important modulator of its long-range transport potential. There  
15 currently exists a large uncertainty in the particle size distribution of iron aerosol, and the role of aerosol size in shaping global  
16 soluble iron deposition is thus unclear. In this study, we couple a sophisticated microphysical, size-resolved aerosol model  
17 with an iron-speciated and -processing module to disentangle the impact of iron emission size distributions on soluble iron  
18 input to the ocean, with a focus on anthropogenic combustion and metal smelting sources. We first evaluate our model results  
19 against a global-scale flight measurement dataset for anthropogenic iron concentration and find that the different  
20 representations of iron size distribution at emission, as adopted in previous studies, introduces a variability in modeled iron  
21 concentrations over remote oceans of a factor of 10. Shifting the iron aerosol size distribution toward finer particle sizes (<1  
22  $\mu\text{m}$ ) enables longer atmospheric lifetime (a doubling), promoting atmospheric processing that enhances the soluble iron  
23 deposition to ocean basins by up to 50% on an annual basis. Importantly, the monthly enhancements reach 110% and 80%  
24 over the Southern Ocean and North Pacific Ocean, respectively. Compared with emission flux uncertainties, we find that iron  
25 emission size distribution plays an equally important role in regulating soluble iron deposition, especially to the remote oceans.  
26 Our findings provide implications for understanding the effects of atmospheric nutrients input on marine biogeochemistry,  
27 including but not limited to iron, phosphorus, and others.



28 **1. Introduction**

29 Iron is a critical micronutrient supporting marine primary production, which is closely associated with marine carbon-nitrogen  
30 cycles in the Earth system [Mahowald *et al.*, 2018; Moore *et al.*, 2001]. The atmospheric deposition of soluble iron to many  
31 ocean basins has long been regarded as an important source of bioavailable iron for ocean biota uptake in iron-limited areas  
32 [Jickells and Moore, 2015; Jickells *et al.*, 2005; Tagliabue *et al.*, 2017]. Understanding the amount and past-to-future evolution  
33 of atmospheric iron deposition to the ocean is critical in assessing the ocean carbon sequestration under a changing climate  
34 [Bergas-Massó *et al.*, 2023; Hamilton *et al.*, 2020a; Myriokefalitakis *et al.*, 2020].

35 The quantification of soluble (bioavailable) iron input to the ocean is linked to differences in iron emission source properties,  
36 the degree to which iron aerosol undergoes acidic or organic chemistry, and atmospheric transport [Hamilton *et al.*, 2022].  
37 Atmospheric iron comes from three major emission sources, i.e., wind-blowing dust, wildfire and biomass burning, and  
38 anthropogenic activities, such as fossil fuel combustion and iron smelting. Dust storms, which frequently occur in arid or semi-  
39 arid regions of the world, such as North Africa and East Asia, provide an abundant iron source to the ocean and support primary  
40 production [Mahowald *et al.*, 2009; Westberry *et al.*, 2023]. In addition, a growing body of evidence is showing that pyrogenic  
41 iron, with higher fractional solubility than dust [Ito *et al.*, 2019], is a large source of atmospheric soluble iron deposition to  
42 many ocean basins, including the Southern Ocean, Northern Pacific Ocean, and Northern Atlantic Ocean [Conway *et al.*, 2019;  
43 Liu *et al.*, 2022; Matsui *et al.*, 2018; Seo and Kim, 2023]. Because the strength of each source could be affected by future  
44 climate change and/or human activities, their contributions to bioavailable iron input to the ocean may vary regionally and  
45 temporally by the end of the century [Bergas-Massó *et al.*, 2023].

46 Atmospheric transport provides the essential pathway in which iron aerosol emitted from the land is supplied to the remote  
47 ocean. Atmospheric circulation patterns dictate the main transport pathways for aerosol to follow and thereby which source  
48 regions are important to consider in terms of their supply to ocean basins. Additionally, atmospheric transport enables internal  
49 mixing of iron-bearing aerosols with other aerosol and gas components, like sulfates and organics; a process commonly known  
50 as aging that facilitates the dissolution of iron from an insoluble state to a soluble state [Li *et al.*, 2017; Shi *et al.*, 2020; Shi *et al.*,  
51 2012; Solmon *et al.*, 2009]. The atmospheric aging processes can significantly increase iron solubility and subsequent  
52 soluble iron deposition, evidenced by both in-field and laboratory observations and global model simulations [Ito, 2015; Li *et al.*,  
53 2017; Longo *et al.*, 2016]. Uncovering the underlying mechanisms of the aging processes and associated enhancement of  
54 iron solubility during transport is an ongoing topic of investigation [Meskhidze *et al.*, 2019; Shi *et al.*, 2020].

55 To elucidate atmospheric flux of iron-containing aerosols to the ocean, atmospheric models have been developed to include a  
56 range of iron emission sources that currently show a large intermodal difference in flux estimates [Myriokefalitakis *et al.*,  
57 2018]. Part of the problem is that it is difficult to realistically reproduce the distribution of soluble iron concentrations across  
58 all the different regions of the world, and especially over the remote polar oceans that are often characterized by low iron  
59 concentrations with a high fractional solubility [Ito *et al.*, 2019]. Note that the size distribution of iron, which is an important  
60 consideration when determining the particle lifetime, and thus its long-range transport potential, is key in atmospheric iron  
61 flux to the ocean [Hamilton *et al.*, 2020b; Myriokefalitakis *et al.*, 2018]. Compared to coarse-sized particles (e.g., larger than  
62 1  $\mu\text{m}$ ), smaller particles generally feature lower loss rates with respect to dry deposition and wet removal, resulting in longer  
63 atmospheric lifetimes; being transported a longer distance increases the potential for atmospheric processing (i.e., longer period  
64 of aerosol ageing) and thus higher soluble iron deposition. Representation of iron size distribution in models could be therefore  
65 important.

66 Iron aerosol characteristics depend in part on differences between source types. The iron mass size distribution associated with  
67 natural dust sources commonly pertains to mineral dust aerosols, with the coarse-sized (diameter greater than 1  $\mu\text{m}$ ) fraction



68 dominant [Albani *et al.*, 2014; Mahowald *et al.*, 2014]. Similarly, fire iron emissions are dominated (>80%) by coarse mode  
69 particles [Hamilton *et al.*, 2019], suggested to be due to the entrainment of local dust iron-bearing aerosol in the pyro convective  
70 updrafts generated by a fire [Hamilton *et al.*, 2022]. For iron aerosol with an anthropogenic source, however, the relative  
71 fractions between the fine and coarse particle size distribution at emission are more divergent among previous investigations.  
72 Recent observational constraints reveal large mass concentrations of anthropogenic iron oxide in the fine mode [Moteki *et al.*,  
73 2017], while a subset of modelling studies have treated most of this iron in the coarse mode [Wang *et al.*, 2015]. As opposed  
74 to those natural sources, anthropogenic iron size distributions may be highly variable with respect to diverse fuels, combustion  
75 temperatures, and industrial processes, as well as the abatement technologies applied to control air pollution [Hamilton *et al.*,  
76 2020b; Rathod *et al.*, 2020].

77 The extent to which iron aerosol size distributions shape the pattern of atmospheric soluble iron inputs to different ocean  
78 regions is currently unknown. Herein, by leveraging a size-resolved global aerosol model configured with iron processes, we  
79 focus on the representation of anthropogenic iron size distributions at emission, primarily involving its roles in altering global  
80 long-range transport and deposition fluxes of iron. We further put the effect of iron size distribution in the context with iron  
81 emission uncertainty to shed light on their relative importance in controlling global-scale iron deposition.

82

## 83 **2. Methods and Materials**

### 84 **2.1 Global aerosol model**

85 We conducted global aerosol simulations using the Community Atmospheric Model version 5 (CAM5.3) with the Aerosol  
86 Two-dimensional bin module for foRmation and Aging Simulation version 2 (CAM-ATRAS) [Matsui, 2017; Matsui and  
87 Mahowald, 2017]. The model treats a series of aerosol chemical and microphysical processes in a size-resolved manner with  
88 12 aerosol size bins from 1 to 10,000 nm in diameter. Our recent study suggests that this size-resolved method can well  
89 represent the growth of small particles to larger ones and the evolution of particle size distributions during atmospheric  
90 transport [Liu and Matsui, 2022]. The improvement of aerosol in-cloud wet scavenging process was included to improve the  
91 modelling of aerosol long-range transport efficiency [Liu and Matsui, 2021]. The CAM-ATRAS model has been adequately  
92 validated for aerosol mass and number concentrations at a global scale using comprehensive measurements from the ground  
93 to the upper troposphere [Gliß *et al.*, 2021; Kawai *et al.*, 2021; Matsui and Liu, 2021; Matsui *et al.*, 2022; Matsui and Moteki,  
94 2020].

95 To represent the iron cycle from emission to deposition, we explicitly treated iron constituents within the aerosol model, similar  
96 to our previous study [Liu *et al.*, 2022], while with updates for iron processing in the current work. All iron-bearing components  
97 were assumed to be internally mixed with other aerosols and underwent emission, physical transport, chemical aging (e.g.,  
98 solubilization), and deposition in the atmosphere. Our model simulated iron solubility and atmospheric processing of iron-  
99 bearing aerosols through the online coupling with the Mechanism of Intermediate complexity for Modelling Iron [Hamilton *et al.*,  
100 2019]. For anthropogenic iron, we consider five different minerals, namely magnetite, hematite, illite, kaolinite, and sulfate  
101 iron, following the global emission inventory by Rathod *et al.* [2020]. We account for a wide range of anthropogenic sources  
102 including iron smelting and fossil fuel combustion sources taken into account. Dust iron emission was calculated by assuming  
103 a constant iron content of 3.5% in dust aerosol emission [Shi *et al.*, 2012]. The global interannual mean iron (insoluble +  
104 soluble) emissions from dust, biomass burning, and anthropogenic sources were 87 Tg Fe yr<sup>-1</sup>, 1.1 Tg Fe yr<sup>-1</sup>, and 2.2 Tg Fe  
105 yr<sup>-1</sup>, respectively.



106 We validated our modeled anthropogenic iron oxide concentrations against a global-scale aircraft measurement in the  
107 troposphere consisting of eight campaigns for the periods of 2009–2011 and 2016–2018 [Lamb *et al.*, 2021]. These  
108 observations include iron oxide aerosols with volume equivalent diameters between 180–1290 nm. The model results were  
109 extracted along the flight tracks in time and space and further averaged in several latitudinal bands across Pacific and Atlantic  
110 Oceans (see Fig. S1). More details can be seen in Liu *et al.* [2022].

111 The model was compiled with a horizontal resolution of  $1.9^\circ \times 2.5^\circ$  (latitude  $\times$  longitude) and 30 vertical layers from the  
112 surface to 40 km. We ran the model for the two periods, 2008–2011 and 2015–2018, with the first year in each period as spin-  
113 up. The meteorological fields were nudged by the Modern-Era Retrospective analysis for Research and Applications Version  
114 2. In addition, to provide implications for ocean biogeochemistry, we estimated the changes in marine net primary production  
115 induced by iron inputs following the methods used by Rathod *et al.* [2022] and Okin *et al.* [2011], in which a cut-off ( $4 \mu\text{mol}$   
116  $\text{L}^{-1}$ ) of nitrate concentrations at surface water was chosen to define the geographical areas of iron-limited ocean basins.

## 117 2.2 Representation of iron size distribution

118 The number and mass size distribution of aerosol at emission is an essential parameter in aerosol modelling. However, due to  
119 the limited knowledge about iron emission characteristics, the representation of iron size distributions varies greatly for  
120 anthropogenic sources. We tested four different size distributions of anthropogenic iron at emission (Fig. 1), briefly described  
121 as follows.

122 First, we adopted the same size distribution with our previous studies [Liu *et al.*, 2022; Matsui *et al.*, 2018] based on Moteki  
123 *et al.* [2017], abbreviated as Moteki2017 hereafter, which was derived from a power law function to fit the observed  
124 anthropogenic iron oxides concentrations within the boundary layer in the outflow of East Asian sources. Note that the  
125 observed size-resolved number concentrations were confined within 170 to 2,100 nm in diameter given the detection limit. By  
126 extrapolating the observation results, we obtained the mass size distribution between 1 nm and 10,000 nm with negative values  
127 excluded. In this case, more than 90% of iron mass was allocated to the size range of 100 nm to 2,500 nm. In addition, we  
128 varied the emissions by a factor of two ( $\times 0.5$  and  $\times 2.0$ , respectively) in another two parallel experiments to account for the  
129 potential uncertainties in iron emission estimates.

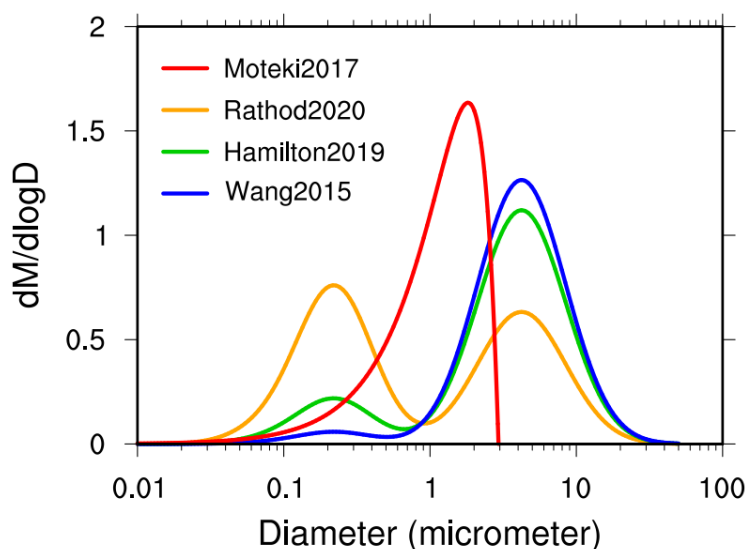
130 The second case was derived from Rathod *et al.* [2020] (abbreviated as Rathod2020 hereafter). They developed a new  
131 mineralogy-based iron emission inventory by introducing more details in anthropogenic sources, especially the inclusion of a  
132 metal smelting source. These improvements increase the fine aerosol (less than  $1 \mu\text{m}$  in diameter) fractions by a factor of 10  
133 higher than most previous inventories. Consequently, this inventory was characterized with almost equal fractions between  
134 fine- and coarse-sized emissions, while previous inventories always applied a much larger fraction for the coarse mode.  
135 Consistent with Rathod *et al.*, we allocated 10% and 90% of fine iron mass to the Aitken mode and the accumulation modes  
136 of aerosols, respectively.

137 The third case was derived from Hamilton *et al.* [2019] (abbreviated as Hamilton2019 hereafter). They revised the  
138 anthropogenic iron emission inventory based on Luo *et al.* [2008] (no metal smelting) and showed that the ratio of fine-sized  
139 iron mass with that of the coarse-sized was 1:5.6, which resulted in the coarse mode dominating. A similar ratio for  
140 anthropogenic iron emissions was applied by Ito [2013]. Also, 10% of fine-sized emissions were allocated to the Aitken mode  
141 and the remaining 90% to the accumulation mode.

142 The fourth case was derived from Wang *et al.* [2015] (abbreviated as Wang2015 hereafter). In their combustion-iron inventory,  
143 the ratio of fine-mode mass to the coarse mode was as low as 1:24, because only 0.1–0.3 % of iron mass from coal fly ash  
144 were emitted in the fine mode. Thus, we allocate 96% of iron in the coarse mode and the remaining 4% in the fine mode.



145 To enable the intercomparison among these cases, we used the global-scale anthropogenic iron emission mass inventory from  
 146 *Rathod et al.* [2020] but with different allocations between fine and coarse sizes in each case. Therefore, the simulated  
 147 variability in atmospheric iron input to the ocean between cases should be attributable to iron size distributions rather than  
 148 emission amount. For the last three cases, we adopted three constant log-normal modes to distribute iron emissions, namely  
 149 Aitken, accumulation, and coarse modes, with their determining parameters including geometric standard deviations, number  
 150 mode diameter, and density reported by *Hamilton et al.* [2019]. We then separated these three modes into 12 size bins from 1  
 151 nm to 10,000 nm adapted for our size-resolved aerosol modelling. The size distributions of iron from biomass burning and  
 152 dust sources were consistent with *Liu et al.* [2022] in all cases. In the following analysis, we grouped the Moteki2017 and  
 153 Rathod2020 as the fine-sized group while the Hamilton2019 and Wang2015 as the coarse-sized group.



154  
 155 **Fig. 1.** Mass size distribution functions for anthropogenic iron emission adopted in four previous studies. The Moteki2017  
 156 curve was provided by fitting in-situ measurements for iron particles within the range of 170 and 2,100 nm in diameter over  
 157 East Asia; the Rathod2020 was based on the latest combustion iron emission inventory, with updates on iron estimate in fine-  
 158 mode sizes (<1 $\mu$ m); the Hamilton2019 and Wang2015 cases were modeling studies that assumed most anthropogenic  
 159 combustion in the coarse-mode bin.

160

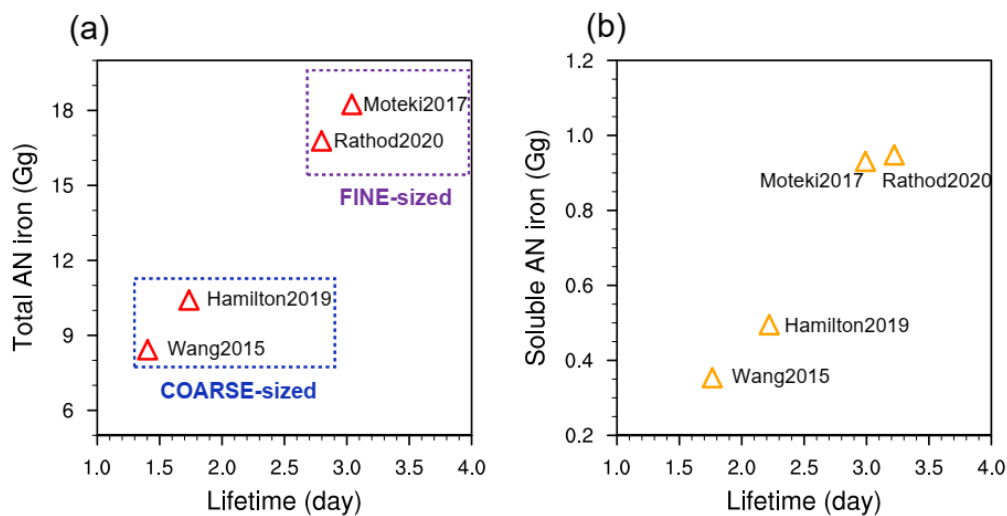
### 161 3. Results and Discussion

#### 162 3.1 Atmospheric iron aerosol concentrations

163 We first examined the effect of changes to iron particle size distributions for anthropogenic sources (unless otherwise stated)  
 164 on the atmospheric iron aerosol burden and its global distributions. Figure 2 illustrates that the global-mean anthropogenic  
 165 iron lifetimes differ by about a factor of 2 among the four examined cases. Both the Moteki2017 and Rathod2020 cases  
 166 simulated a lifetime around 3.0 days. In contrast, the Hamilton2019 and Wang2015 cases simulated a lifetime around half as  
 167 long (between 1.4 and 1.7 days). As only the size distribution is changed in these simulations the change in lifetime is directly  
 168 linked to the apportionment of mass aerosol between fine and coarse particle size modes. This result is in line with previous  
 169 reports [*Hamilton et al.*, 2020b], and demonstrates that shifting emitted iron toward fine-sized diminishes atmospheric loss  
 170 rates of iron aerosols via dry (sedimentation) and wet (precipitation) removal pathways and extends their lifetime.  
 171 Consequently, given the same emission amount, the atmospheric iron burdens are enhanced, accordingly by approximately a  
 172 factor of 2 from ~9.0 Gg in the coarse-sized cases (Hamilton2019 and Wang2015) to ~18.0 Gg in the fine-sized cases



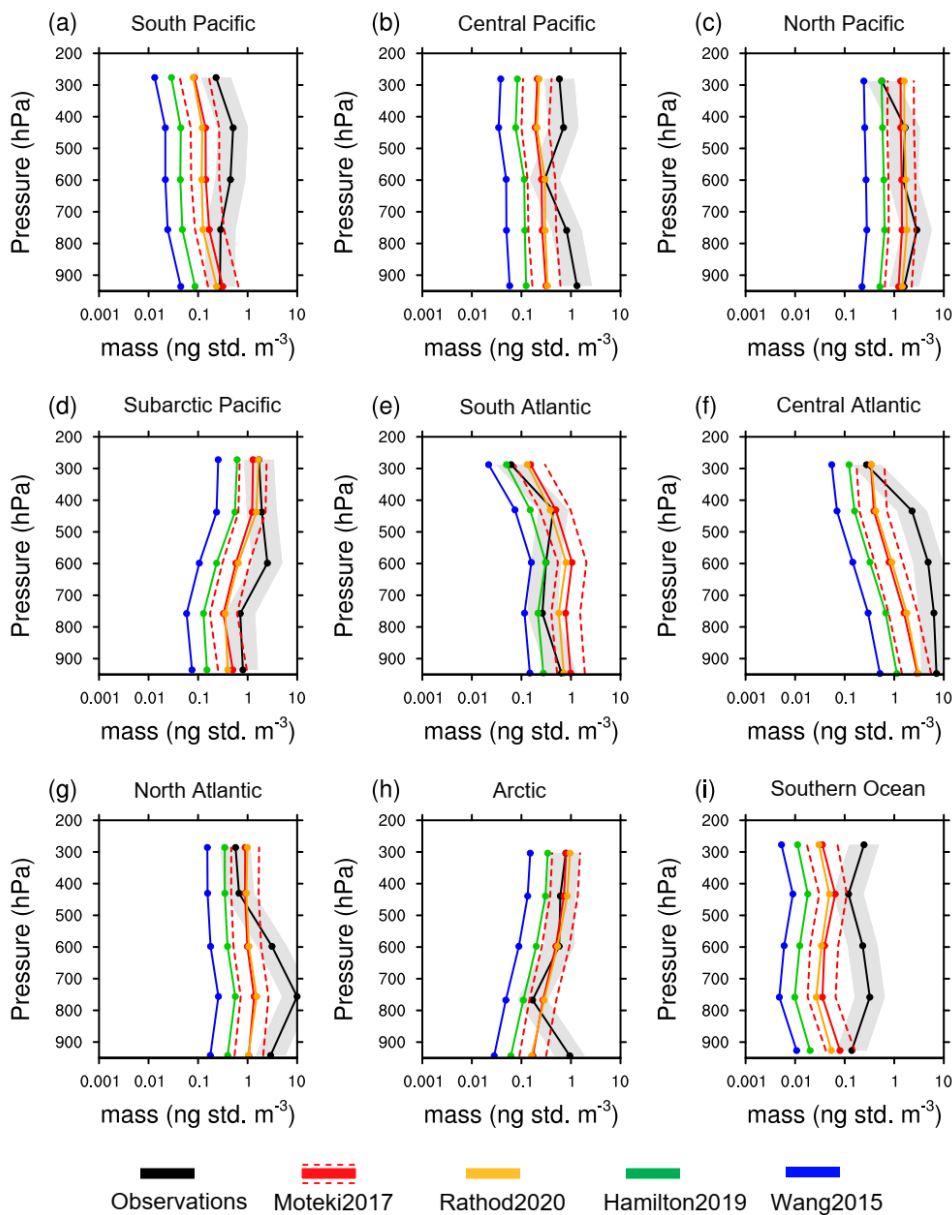
173 (Moteki2017 and Rathod2020). In a similar manner, the lifetimes and mass burdens of anthropogenic iron in the soluble form  
174 are almost doubled in the fine-sized cases (Fig. 2b). The extended lifetimes also enhance the globally averaged iron solubility  
175 (Fig. S2), by allowing more iron subject to aerosol aging and solubilization processes.



176

177 **Fig. 2.** Global anthropogenic iron concentration burdens and lifetimes varied by the emission size distributions. The scatter  
178 plots are shown for (a) anthropogenic iron (labeled as AN iron) burden vs. lifetime and (b) soluble anthropogenic iron vs.  
179 lifetime. Four representative cases are examined in this work: Moteki2017, Rathod2020, Hamilton2019, and Wang2015. The  
180 first two cases are grouped into “FINE-sized” and the other two are grouped into “COARSE-sized”.

181



182

183

184

185

186

187

188

189

190

191

192

193

**Fig. 3.** Comparison of modelled anthropogenic iron mineral (magnetite) vertical concentration profiles in four cases with aircraft measurements across global oceans. The flight routes and model-observation sampling methods have been documented in *Lamb et al.* [2021] and *Liu et al.* [2022]. The geographical location of each oceanic area is marked in Fig. S1. We also scaled up and down emission fluxes by a factor of 2 from the Moteki2017 case, respectively, to account for potential uncertainties in emission estimates (red dashed lines in the panels).

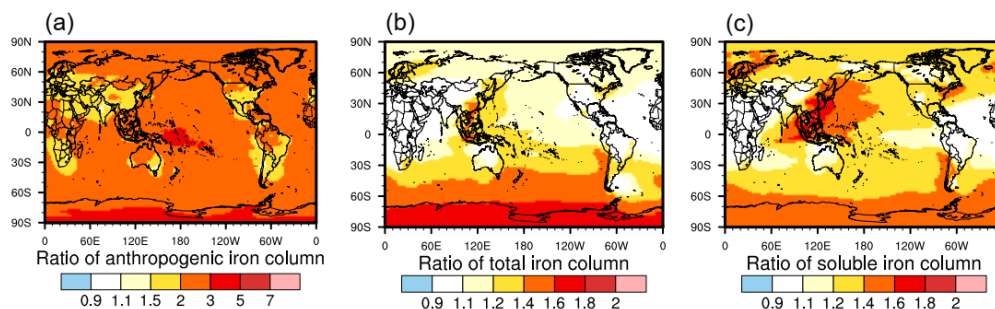
To evaluate each iron simulation, we compare simulated aerosol characteristics against global-scale aircraft measurements of anthropogenic magnetite within nine regions of the troposphere (Fig. 3). The size distribution consistent with the measurements is selected for our model results. Note that magnetite, comprised about 70% of anthropogenic iron emissions, can be used an indicator of anthropogenic iron abundance in the atmosphere [*Matsui et al.*, 2018; *Rathod et al.*, 2020]. Despite the same emission fluxes considered in all cases, their simulated magnetite aerosol concentrations can differ by up to a factor of 10. Specifically, the Moteki2017 and Rathod2020 cases show a much higher performance in reproducing the observed profiles



194 over all ocean basins compared to Hamilton2019 and Wang2015 cases. In particular, the cases with a more uniformly  
 195 distributed particle size distribution across modes captures the high concentration ( $>1 \text{ ng m}^{-3}$ ) in North Pacific, which can be  
 196 linked to atmospheric plumes transported from East Asia with intensive emission rates [Moteki *et al.*, 2017; Seo and Kim,  
 197 2023]. Some underestimations still exist in near-surface or high altitudes. Doubling the emission fluxes based the Moteki2017  
 198 case can appreciably narrow the gaps with the observation (dashed red lines in Fig. 3). In contrast, the coarse-sized dominated  
 199 simulations (i.e., Hamilton2019 and Wang2015) underrepresents the magnetite concentrations over global remote oceans,  
 200 particularly by up to one order of magnitude over the Pacific Ocean. The shorter lifetimes in this group limit the long-range  
 201 transport of iron aerosols from continental sources to the remote atmosphere.

202 These results imply that agreement between observations and model simulations can be improved by reducing uncertainties in  
 203 the emission inventory and in the long-range transport efficiency associated with representation of iron size distributions.  
 204 Moreover, as illustrated in Fig. 3, the variabilities (the ratio between the maximum and minimum) of simulated magnetite  
 205 vertical profiles by iron size distribution changes are wider than those by the emission uncertainties, for which emission fluxes  
 206 were perturbed by a factor of 2 ( $\times 2.0$  and  $\times 0.5$ , respectively) to test the sensitivity of simulated iron concentrations. We  
 207 therefore highlight that in order to observationally constrain iron emissions more realistically in global aerosol simulations, it  
 208 is a prerequisite to use a realistic empirical representation of anthropogenic iron aerosol size distributions.

209



210

211 **Fig. 4.** Global map of variability in iron column concentrations between the fine-sized group and the coarse-sized group. The  
 212 variability ratios (fine-sized/coarse-sized) are calculated for (a) anthropogenic iron, (b) total iron, and (c) soluble iron,  
 213 respectively. Herein, total iron is a combination of iron from dust, biomass burning, and anthropogenic sources, the soluble  
 214 form of which denotes soluble iron. The ratios represent the maximum differences between the fine-sized group (the  
 215 Moteki2017 and Rathod2020 cases) and the coarse-sized group (the Hamilton2019 and Wang2015 cases) and indicate the  
 216 spread of iron simulations.

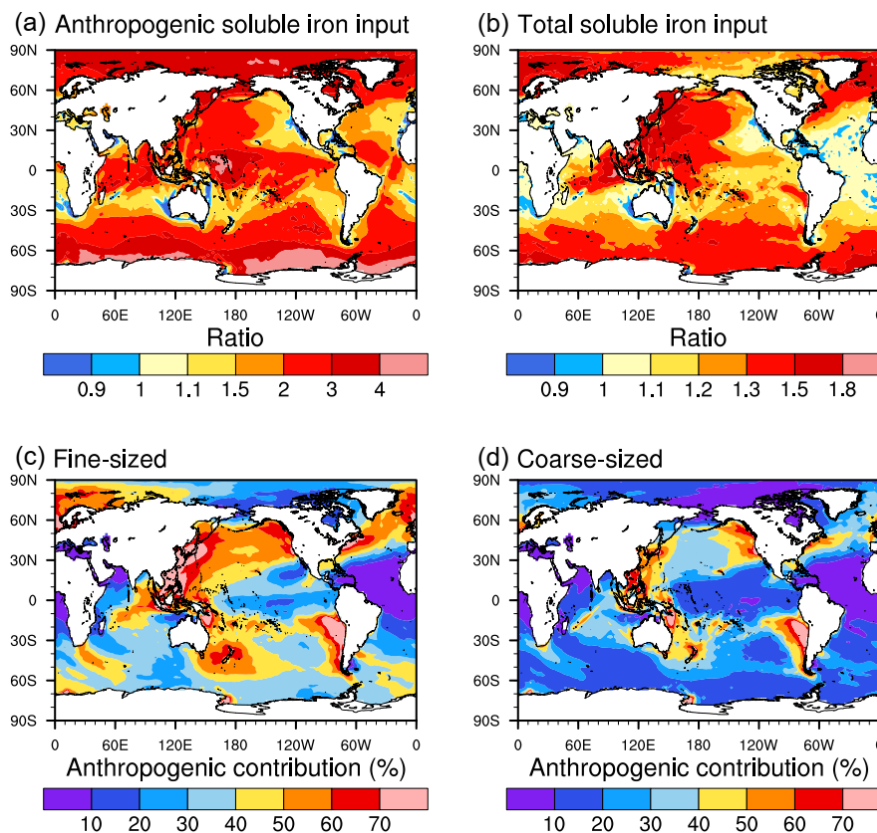
217 Our simulations further demonstrate that the representation of iron size distribution shapes the iron aerosol concentrations at a  
 218 global scale (Fig. 4). Anthropogenic iron in the fine-sized group shows higher column concentrations by more than a factor of  
 219 2 than in the coarse-sized over oceans. The differences (ratios) are larger in those remote oceans compared to source regions  
 220 like East Asia, southern Africa and South America, because iron-bearing aerosols in smaller sizes can be transported to a  
 221 longer distance. The variability between the two groups is much less relative to total iron (Fig. 4b), which also includes  
 222 contributions from dust and biomass burning sources. One exception is the Southern Ocean with still large ratios around 1.5,  
 223 reflecting an important fractional contribution of anthropogenic iron among all sources over this region. Note that the  
 224 differences for soluble iron are more pronounced than for total iron (Fig 4c), because of the higher solubility of anthropogenic  
 225 iron than dust iron. Over East Asia and its outflow areas, the rapid aging process in the polluted environments are capable of  
 226 enhancing iron solubility and thus amplify the differences of soluble iron concentrations between the fine-sized and coarse-  
 227 sized groups [Li *et al.*, 2017; Zhu *et al.*, 2022].

228





229 **3.2 Atmospheric soluble iron input to the ocean**



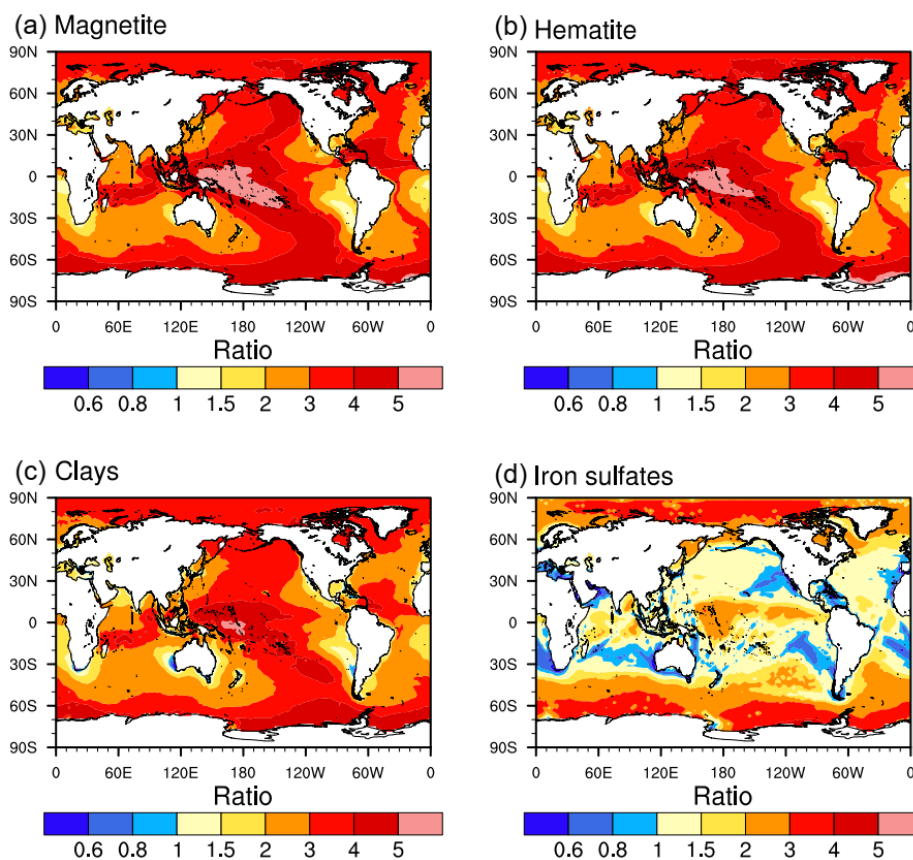
230

231 **Fig. 5.** Comparison of atmospheric soluble iron input to the ocean between the fine-sized and coarse-sized cases. Shown here  
 232 are (a) the ratio of anthropogenic soluble iron simulated in the fine-sized case to the result of the coarse-sized, (b) the ratio of  
 233 total soluble iron, (c) the fractional contribution (in percentage) of anthropogenic emission to total soluble iron input in the  
 234 fine-sized case, and (d) the fractional contribution of anthropogenic emission in the coarse-sized case.

235 Next, we examine the extent to which the iron size distributions at emission can alter soluble iron input to the global ocean  
 236 basins, which is vital to net primary productivity, especially in the high-nutrient, low-chlorophyll (HNLC) areas [Hamilton et  
 237 al., 2022; Moore et al., 2013]. As illustrated in Fig. 5, though the global emission and the resulting annual iron (insoluble +  
 238 soluble) deposition amount are the same between cases, their geographical distributions vary substantially. Using the ratio of  
 239 annual soluble iron deposition in the fine-sized group to that of the coarse-sized as a proxy of the variability, we find the fine-  
 240 sized distributions lead to much more soluble iron input to remote ocean basins including North Pacific and Southern Ocean,  
 241 by up to a factor of 4 for the anthropogenic sources and 1.5 for the total of all sources (i.e., anthropogenic + fire + dust). Similar  
 242 spatial patterns emerge regarding the total iron deposition, suggesting the importance of long-range transport efficiency in  
 243 regulating iron distributions (Fig. S3). The variability is negligible in the equatorial and subtropical Atlantic, where dust iron  
 244 dominates soluble iron input to this area. The ratios less than 1, indicating reduced deposition fluxes in the fine-sized group,  
 245 are found near the continental sources, including western U.S., Australia, and southern Africa, because of the slower deposition  
 246 speed. However, in East Asia, which has most intensive anthropogenic iron emissions, the shift toward finer sizes also increase  
 247 soluble iron deposition near the sources (e.g., eastern China). This is attributable to the rapid aging processes of the fine-sized  
 248 iron in such polluted environment that convert more insoluble iron to its soluble form [Baldo et al., 2022; Zhang et al., 2022].



249 The source appointment of soluble iron deposition across ocean basins also varies with iron size distributions (Fig. 5c-d). The  
 250 anthropogenic iron emission becomes more dominant in North Pacific, North Atlantic, and parts of the Southern Ocean, with  
 251 its fractional contribution reaching more than 50% in the fine-sized group compared to that of 30–40% in the coarse-sized.  
 252 Such variability is attributable to the enhancement of anthropogenic soluble iron fluxes to those remote oceans by the shift of  
 253 anthropogenic iron emission toward finer size bins. Globally, the soluble iron deposition from anthropogenic sources is 55.0  
 254 Gg per year for the fine-sized group, larger than that of 35.3 Gg per year for the coarse-sized group. Hence, even though the  
 255 same emission is applied in these simulations, the diversity of iron size distributions at emission yields a considerable  
 256 variability of soluble iron deposition on a global basis. As discussed earlier, the extended iron lifetime by about a factor of 2  
 257 in the fine-sized group allows more iron to be transported to a remote region and simultaneously increases the amount of  
 258 atmospheric iron processing and dissolution to a soluble form. Of the total iron deposition, the soluble fraction is thus notably  
 259 elevated. We also find that the chemical aging process, as the major source of soluble iron, controls the differences of soluble  
 260 iron deposition over remote oceans between the fine-sized and coarse-sized groups (Fig. S4).

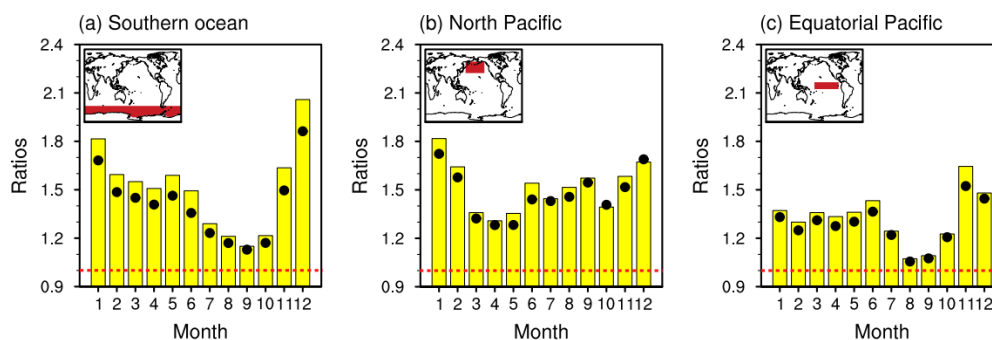


261  
 262 **Fig. 6.** Ratios of soluble iron deposition from four anthropogenic iron-containing minerals between the fine-sized and coarse-  
 263 sized cases.

264 In this study, the explicit treatment of anthropogenic iron mineralogy enables us to identify the iron mineral-dependent  
 265 variability. We find that for those coming primarily from fossil fuel combustion and iron smelting on land, namely magnetite,  
 266 hematite, and clays, the shift of iron emissions toward finer size bins promotes their long-range transport and enhances  
 267 corresponding soluble iron deposition to North Pacific, Equatorial Pacific, and Southern Ocean by more than a factor of 4 (Fig.  
 268 6a-c). However, the size distribution effects on iron sulfates are pronounced only in the polar areas, which are subject to plumes

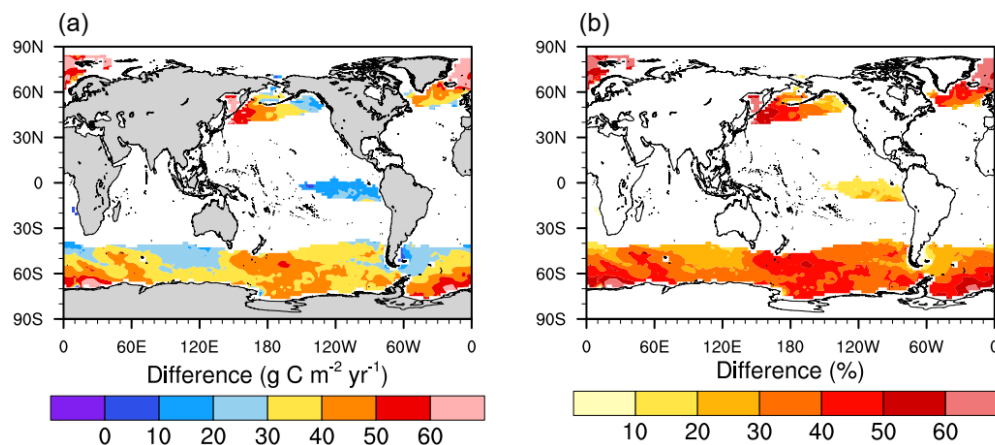


269 of middle latitude shipping emissions. In line with previous study [Rathod *et al.*, 2022], the iron sulfates constitute an important  
 270 contribution to soluble iron deposition away from major continental sources, predominately associated with shipping emission  
 271 over local oceans rather than long-range transport from land (Fig. S5). Hence, the variability induced by iron size distributions  
 272 is less remarkable for iron sulfates than for other anthropogenic minerals. These results also suggest that the relative importance  
 273 of iron sulfates in total soluble iron deposition to remote oceans is altered by the size distributions of all other iron minerals  
 274 that originate from continental sources.



275  
 276 **Fig. 7.** Differences of monthly total soluble iron deposition between the fine-sized and coarse-sized groups over specific ocean  
 277 basins. Only anthropogenic iron emission sizes have been examined here. Histograms describe the ratio of monthly results in  
 278 the fine-sized case to that of the coarse-sized for (a) Southern Ocean, (b) North Pacific, and (c) Equatorial Pacific, respectively.  
 279 For comparison, black dots describe the ratio of the fine-sized results to that with global anthropogenic emission amount  
 280 scaling down by a factor of 2. The ocean basins of interest are indicated at the top-left corner of each panel. The red dashed  
 281 lines indicate the ratio of 1.0.

282 It is critical to examine monthly soluble iron availability altered by emission size distributions, because ocean primary  
 283 production can respond to iron inputs on the order of days to months [Guieu *et al.*, 2014]. From our results in Fig. 7, the  
 284 importance of anthropogenic emission size distributions in shifting soluble iron deposition varies by month over potentially  
 285 iron-limited ocean basins, i.e., HNLC regions, due to the episodic nature of natural iron sources (dust and wildfire) and their  
 286 deposition. For the Southern Ocean, the monthly ratios of the fine-sized case to the coarse-sized span from 1.1 in September  
 287 to 2.1 in December (Fig. 7a). The September peak of fire iron (shown in Fig. S6), possibly linked to low precipitation in  
 288 southern winter, masks the variability in anthropogenic iron contributions by emission size distributions. Conversely, the  
 289 largest difference in December is associated with the lowest contribution of natural sources (Fig. S6). By contrast, the monthly  
 290 differences are less fluctuated in North Pacific, ranging between 1.3 and 1.8 (Fig. 7b). Anthropogenic emission dominates  
 291 soluble iron throughout the year except in March-May, during which dust storms originating from East Asia frequently occur  
 292 and regulate soluble iron inputs to North Pacific. The Equatorial Pacific has the lowest ratio amongst the three regions, because  
 293 anthropogenic aerosol bearing plumes rarely arrive in this region and lots of rain out here can efficiently remove aerosols.  
 294 For the three ocean basins, such differences related to the emission size treatments are even larger than those by adjusting the iron  
 295 emission amount by a factor of 2 with the consideration of emission uncertainty (black dots in Fig. 7). We therefore suggest  
 296 that compared with iron emission fluxes, the representation of size distributions for anthropogenic iron is equally or even more  
 297 important to the estimation of total soluble iron deposition to remote oceans.



298

299 **Fig. 8.** Difference of marine net primary production sustained by atmospheric soluble iron between two iron size distribution  
 300 groups. Here, following *Rathod et al.* [2022], we focus only on the iron-limited ocean basins, which are defined using a cut-  
 301 off of nitrate concentrations at surface oceans.

302 We also provide an estimate of the changes in iron-sustained marine net primary production between the finer-sized and coarse-  
 303 sized groups (Fig. 8). In line with the distributions of soluble iron deposition, the effects of finer-sized iron distributions can  
 304 enhance primary production over remote oceans including the North Pacific Ocean and Southern Ocean as high as 50%.  
 305 Considering that anthropogenic iron aerosols may contribute to >10% of the total marine productivity in the North Pacific  
 306 Ocean [*Ito et al.*, 2020; *Rathod et al.*, 2022], the representation of their size distributions at emissions, mostly from East Asia,  
 307 is particularly important in the Earth system modeling. The evolution of atmospheric iron-aerosol size characteristics and their  
 308 emission fluxes can be critical players to ocean carbon sequestration from past to future. *Hamilton et al.* (2020) found that  
 309 historical air pollution controls has cut down anthropogenic emission amounts of particles in coarse sizes, in turn elevating the  
 310 mass fraction of finer-sized iron particles and thus the overall lifetime of atmospheric iron. Hence, the complex interactions of  
 311 iron and the Earth system is linked to human activity effects on soluble iron availability to ocean basins.

312

#### 313 4. Conclusion

314 This study explores the extent to which iron size distribution at emission, specifically from anthropogenic sources, alters  
 315 estimates of soluble iron deposition to the open ocean. A global microphysical, size-resolved aerosol model is used to simulate  
 316 the iron cycle, involving emission, atmospheric processing, and deposition on a global scale. The model treats iron mineralogy,  
 317 size evolution, and chemical aging processes during atmospheric transport, which enables the investigation on the relationship  
 318 between iron size distributions and iron long-range transport and subsequent deposition. We test four representative size  
 319 distribution schemes for anthropogenic iron sources employed in previous studies.

320 We find that allocating a more balanced fraction of iron aerosol at emission into particle sizes less than 1  $\mu\text{m}$ , results in a longer  
 321 atmospheric lifetime and mass burden of total iron aerosols by about a factor of 2 compared to a coarse-sized dominated case,  
 322 primarily associated with the decreased loss rates via dry and wet removal processes. The evaluation of anthropogenic iron  
 323 aerosols against the global-scale observation dataset reveals that despite the same emission fluxes considered in all cases, their  
 324 simulated magnetite aerosol concentrations differ by up to a factor of 10, while the higher fine-sized cases agree better with  
 325 the observations. It is therefore necessary to accurately represent iron size distributions in order to constrain iron emission  
 326 fluxes more realistically with aerosol simulations and observations [*Liu et al.*, 2022]. Our simulations show that the resulting  
 327 annual soluble iron deposition differs by up to a factor of 1.5 over remote oceans including the North Pacific Ocean and



328 Southern Ocean, because the fine-sized group allows more iron to be transported to a long distance with enhanced atmospheric  
329 processing. More importantly, the monthly soluble iron deposition, which is relevant to ocean primary production responses  
330 over days to months, would be enhanced by 110% and 80% in the fine-sized case over the Southern Ocean and North Pacific  
331 Ocean, respectively. Such differences are similar to or even larger than those with the consideration of emission uncertainty,  
332 suggesting the equally important role of iron size distribution treatment.

333 This study unravels the critical role of iron size distributions in shaping atmospheric soluble iron inputs to global oceans,  
334 especially to the remote regions. However, the realistic understanding of iron emission size distributions is still inadequate  
335 given limited observation data. Targeted in-site measurements on iron aerosol size along with its mass and solubility at source  
336 areas are highly desirable. Furthermore, our finding may be extended to other key trace elements of importance to ocean  
337 biogeochemistry, like copper, manganese, and phosphorus.

338

339 **Author contributions:** H.M. and M.L. designed the research. M.L. performed model simulations, analyzed the data, and wrote  
340 the original manuscript. M.L., H.M., D.S.H., S.D.R., K.D.L., and N.M.M. interpreted the results and discussed their  
341 implications. All authors commented on and contributed to the manuscript.

342 **Competing interests:** The authors declare that they have no conflict of interest.

343 **Data availability:** The model data used to generate the figures can be available after the acceptance of the manuscript.

344 **Code availability:** The CESM source code is publicly available from NCAR at: <https://www.cesm.ucar.edu/>.

#### 345 **Acknowledgement**

346 This study was supported by the Ministry of Education, Culture, Sports, Science, and Technology and the Japan Society for  
347 the Promotion of Science (MEXT/JSPS) KAKENHI Grants (JP20H00196, JP22H03722, JP22F22092, JP22KF0165,  
348 JP23H00515, JP23H00523, JP23K18519, JP23K24976, and JP24H02225); by the MEXT Arctic Challenge for Sustainability  
349 II (ArCS II) Project (JPMXD1420318865); and by the Environment Research and Technology Development Fund 2–2003  
350 (JPMEERF20202003) and 2–2301 (JPMEERF20232001) of the Environmental Restoration and Conservation Agency.  
351 Mingxu Liu acknowledged the support of JSPS Postdoctoral Fellowships for Research in Japan (Standard). DSH was supported  
352 by NASA (Proposal Number: 22-IDS22-0027). We acknowledged the NASA Radiation Sciences Program, the NASA Upper  
353 Atmosphere Research Program, and the NOAA Atmospheric Composition and Climate Program for providing the aircraft  
354 observational data.

355

#### 356 **References:**

- 357 Albani, S., N. M. Mahowald, A. T. Perry, R. A. Scanza, C. S. Zender, N. G. Heavens, V. Maggi, J. F. Kok, and B. L. Otto-  
358 Bliesner (2014), Improved dust representation in the Community Atmosphere Model, *J. Adv. Model. Earth Syst.*, 6(3),  
359 541-570, doi:<https://doi.org/10.1002/2013MS000279>.
- 360 Baldo, C., A. Ito, M. D. Krom, W. Li, T. Jones, N. Drake, K. Ignatyev, N. Davidson, and Z. Shi (2022), Iron from coal  
361 combustion particles dissolves much faster than mineral dust under simulated atmospheric acidic conditions, *Atmos. Chem.*  
362 *Phys.*, 22(9), 6045-6066, doi:10.5194/acp-22-6045-2022.
- 363 Bergas-Massó, E., M. Gonçalves Ageitos, S. Myriokefalitakis, R. L. Miller, T. van Noije, P. Le Sager, G. Montané Pinto, and  
364 C. Pérez García-Pando (2023), Pre-Industrial, Present and Future Atmospheric Soluble Iron Deposition and the Role of  
365 Aerosol Acidity and Oxalate Under CMIP6 Emissions, *Earth's Future*, 11(6), doi:10.1029/2022ef003353.
- 366 Conway, T. M., D. S. Hamilton, R. U. Shelley, A. M. Aguilar-Islas, W. M. Landing, N. M. Mahowald, and S. G. John (2019),  
367 Tracing and constraining anthropogenic aerosol iron fluxes to the North Atlantic Ocean using iron isotopes, *Nat Commun*,  
368 10(1), 2628, doi:10.1038/s41467-019-10457-w.



- 369 Gliß, J., et al. (2021), AeroCom phase III multi-model evaluation of the aerosol life cycle and optical properties using ground-  
370 and space-based remote sensing as well as surface in situ observations, *Atmos. Chem. Phys.*, 21(1), 87-128,  
371 doi:10.5194/acp-21-87-2021.
- 372 Guieu, C., et al. (2014), The significance of the episodic nature of atmospheric deposition to Low Nutrient Low Chlorophyll  
373 regions, *Global Biogeochem. Cycles*, 28(11), 1179-1198, doi:<https://doi.org/10.1002/2014GB004852>.
- 374 Hamilton, D. S., et al. (2020a), Impact of Changes to the Atmospheric Soluble Iron Deposition Flux on Ocean Biogeochemical  
375 Cycles in the Anthropocene, *Global Biogeochem. Cycles*, 34(3), e2019GB006448, doi:10.1029/2019gb006448.
- 376 Hamilton, D. S., et al. (2022), Earth, Wind, Fire, and Pollution: Aerosol Nutrient Sources and Impacts on Ocean  
377 Biogeochemistry, 14(1), 303-330, doi:10.1146/annurev-marine-031921-013612.
- 378 Hamilton, D. S., et al. (2019), Improved methodologies for Earth system modelling of atmospheric soluble iron and observation  
379 comparisons using the Mechanism of Intermediate complexity for Modelling Iron (MIMI v1.0), *Geosci. Model Dev.*,  
380 12(9), 3835-3862, doi:10.5194/gmd-12-3835-2019.
- 381 Hamilton, D. S., R. A. Scanza, S. D. Rathod, T. C. Bond, J. F. Kok, L. Li, H. Matsui, and N. M. Mahowald (2020b), Recent  
382 (1980 to 2015) Trends and Variability in Daily - to - Interannual Soluble Iron Deposition from Dust, Fire, and  
383 Anthropogenic Sources, *Geophys. Res. Lett.*, 47(17), e2020GL089688, doi:10.1029/2020gl089688.
- 384 Ito, A. (2013), Global modeling study of potentially bioavailable iron input from shipboard aerosol sources to the ocean, *Global  
385 Biogeochem. Cycles*, 27(1), 1-10, doi:<https://doi.org/10.1029/2012GB004378>.
- 386 Ito, A. (2015), Atmospheric Processing of Combustion Aerosols as a Source of Bioavailable Iron, *Environ. Sci. Technol. Lett.*,  
387 2(3), 70-75, doi:10.1021/acs.estlett.5b00007.
- 388 Ito, A., et al. (2019), Pyrogenic iron: The missing link to high iron solubility in aerosols, *Sci. Adv.*, 5(5), eaau7671,  
389 doi:10.1126/sciadv.aau7671.
- 390 Ito, A., Y. Ye, A. Yamamoto, M. Watanabe, and M. N. Aita (2020), Responses of ocean biogeochemistry to atmospheric  
391 supply of lithogenic and pyrogenic iron-containing aerosols, *Geol. Mag.*, 157(5), 741-756,  
392 doi:10.1017/S0016756819001080.
- 393 Jickells, T., and C. M. Moore (2015), The Importance of Atmospheric Deposition for Ocean Productivity, *Annu. Rev. Ecol.  
394 Evol. Syst.*, 46(1), 481-501, doi:10.1146/annurev-ecolsys-112414-054118.
- 395 Jickells, T. D., et al. (2005), Global Iron Connections Between Desert Dust, Ocean Biogeochemistry, and Climate, *Science*,  
396 308(5718), 67, doi:10.1126/science.1105959.
- 397 Kawai, K., H. Matsui, and Y. Tobo (2021), High Potential of Asian Dust to Act as Ice Nucleating Particles in Mixed-Phase  
398 Clouds Simulated With a Global Aerosol-Climate Model, *J. Geophys. Res.-Atmos.*, 126(12), e2020JD034263,  
399 doi:<https://doi.org/10.1029/2020JD034263>.
- 400 Lamb, K. D., H. Matsui, J. M. Katich, A. E. Perring, J. R. Spackman, B. Weinzierl, M. Dollner, and J. P. Schwarz (2021),  
401 Global-scale constraints on light-absorbing anthropogenic iron oxide aerosols, *npj Clim. Atmos. Sci.*, 4(1),  
402 doi:10.1038/s41612-021-00171-0.
- 403 Li, W., et al. (2017), Air pollution-aerosol interactions produce more bioavailable iron for ocean ecosystems, *Sci. Adv.*, 3(3),  
404 e1601749, doi:10.1126/sciadv.1601749.
- 405 Liu, M., and H. Matsui (2021), Improved Simulations of Global Black Carbon Distributions by Modifying Wet Scavenging  
406 Processes in Convective and Mixed-Phase Clouds, *J. Geophys. Res.-Atmos.*, 126(3), e2020JD033890,  
407 doi:<https://doi.org/10.1029/2020JD033890>.
- 408 Liu, M., and H. Matsui (2022), Secondary Organic Aerosol Formation Regulates Cloud Condensation Nuclei in the Global  
409 Remote Troposphere, *Geophys. Res. Lett.*, 49(18), doi:10.1029/2022gl100543.
- 410 Liu, M., H. Matsui, D. S. Hamilton, K. D. Lamb, S. D. Rathod, J. P. Schwarz, and N. M. Mahowald (2022), The  
411 underappreciated role of anthropogenic sources in atmospheric soluble iron flux to the Southern Ocean, *npj Clim. Atmos.  
412 Sci.*, 5(1), doi:10.1038/s41612-022-00250-w.
- 413 Longo, A. F., Y. Feng, B. Lai, W. M. Landing, R. U. Shelley, A. Nenes, N. Mihalopoulos, K. Violaki, and E. D. Ingall (2016),  
414 Influence of Atmospheric Processes on the Solubility and Composition of Iron in Saharan Dust, *Environ. Sci. Technol.*,  
415 50(13), 6912-6920, doi:10.1021/acs.est.6b02605.
- 416 Luo, C., N. Mahowald, T. Bond, P. Y. Chuang, P. Artaxo, R. Siefert, Y. Chen, and J. Schauer (2008), Combustion iron  
417 distribution and deposition, *Global Biogeochem. Cycles*, 22(1), GB1012, doi:<https://doi.org/10.1029/2007GB002964>.
- 418 Mahowald, N., S. Albani, J. F. Kok, S. Engelstaeder, R. Scanza, D. S. Ward, and M. G. Flanner (2014), The size distribution  
419 of desert dust aerosols and its impact on the Earth system, *Aeolian Res.*, 15, 53-71,  
420 doi:<https://doi.org/10.1016/j.aeolia.2013.09.002>.
- 421 Mahowald, N. M., et al. (2009), Atmospheric Iron Deposition: Global Distribution, Variability, and Human Perturbations,  
422 *Annual Review of Marine Science*, 1(1), 245-278, doi:10.1146/annurev.marine.010908.163727.
- 423 Mahowald, N. M., D. S. Hamilton, K. R. M. Mackey, J. K. Moore, A. R. Baker, R. A. Scanza, and Y. Zhang (2018), Aerosol  
424 trace metal leaching and impacts on marine microorganisms, *Nat. Commun.*, 9(1), 2614, doi:10.1038/s41467-018-04970-  
425 7.
- 426 Matsui, H. (2017), Development of a global aerosol model using a two-dimensional sectional method: 1. Model design, *J. Adv.  
427 Model. Earth Syst.*, 9(4), 1921-1947, doi:10.1002/2017ms000936.
- 428 Matsui, H., and M. Liu (2021), Importance of Supersaturation in Arctic Black Carbon Simulations, *J. Clim.*, 34(19), 7843-  
429 7856, doi:10.1175/jcli-d-20-0994.1.
- 430 Matsui, H., and N. Mahowald (2017), Development of a global aerosol model using a two-dimensional sectional method: 2.  
431 Evaluation and sensitivity simulations, *J. Adv. Model. Earth Syst.*, 9(4), 1887-1920, doi:10.1002/2017ms000937.



- 432 Matsui, H., N. M. Mahowald, N. Moteki, D. S. Hamilton, S. Ohata, A. Yoshida, M. Koike, R. A. Scanza, and M. G. Flanner  
433 (2018), Anthropogenic combustion iron as a complex climate forcer, *Nat. Commun.*, 9(1), 1593, doi:10.1038/s41467-  
434 018-03997-0.
- 435 Matsui, H., T. Mori, S. Ohata, N. Moteki, N. Oshima, K. Goto-Azuma, M. Koike, and Y. Kondo (2022), Contrasting source  
436 contributions of Arctic black carbon to atmospheric concentrations, deposition flux, and atmospheric and snow radiative  
437 effects, *Atmos. Chem. Phys. Discuss.*, 2022, 1-31, doi:10.5194/acp-2021-1091.
- 438 Matsui, H., and N. Moteki (2020), High sensitivity of Arctic black carbon radiative effects to subgrid vertical velocity in  
439 aerosol activation, *Geophys. Res. Lett.*, 47, e2020GL088978, doi:10.1029/2020GL088978.
- 440 Meskhidze, N., et al. (2019), Perspective on identifying and characterizing the processes controlling iron speciation and  
441 residence time at the atmosphere-ocean interface, *Mar. Chem.*, 217, 103704,  
442 doi:<https://doi.org/10.1016/j.marchem.2019.103704>.
- 443 Moore, C. M., et al. (2013), Processes and patterns of oceanic nutrient limitation, *Nat. Geosci.*, 6(9), 701-710,  
444 doi:10.1038/ngeo1765.
- 445 Moore, J. K., S. C. Doney, D. M. Glover, and I. Y. Fung (2001), Iron cycling and nutrient-limitation patterns in surface waters  
446 of the World Ocean, *Deep Sea Res. Part II*, 49(1), 463-507, doi:[https://doi.org/10.1016/S0967-0645\(01\)00109-6](https://doi.org/10.1016/S0967-0645(01)00109-6).
- 447 Moteki, N., K. Adachi, S. Ohata, A. Yoshida, T. Harigaya, M. Koike, and Y. Kondo (2017), Anthropogenic iron oxide aerosols  
448 enhance atmospheric heating, *Nat. Commun.*, 8(1), 15329, doi:10.1038/ncomms15329.
- 449 Myriokefalitakis, S., M. Gröger, J. Hieronymus, and R. Döscher (2020), An explicit estimate of the atmospheric nutrient  
450 impact on global oceanic productivity, *Ocean Sci.*, 16(5), 1183-1205, doi:10.5194/os-16-1183-2020.
- 451 Myriokefalitakis, S., et al. (2018), Reviews and syntheses: the GESAMP atmospheric iron deposition model intercomparison  
452 study, *Biogeosciences*, 15(21), 6659-6684, doi:10.5194/bg-15-6659-2018.
- 453 Okin, G. S., et al. (2011), Impacts of atmospheric nutrient deposition on marine productivity: Roles of nitrogen, phosphorus,  
454 and iron, *Global Biogeochem. Cycles*, 25(2), doi:<https://doi.org/10.1029/2010GB003858>.
- 455 Rathod, S. D., D. S. Hamilton, L. Li, N. M. Mahowald, H. Matsui, J. R. Pierce, and T. C. Bond (2022), Atmospheric Radiative  
456 and Oceanic Biological Productivity Responses to Increasing Anthropogenic Combustion-Iron Emission in the 1850–  
457 2010 Period, *Geophys. Res. Lett.*, 49(16), doi:10.1029/2022gl099323.
- 458 Rathod, S. D., D. S. Hamilton, N. M. Mahowald, Z. Klimont, J. J. Corbett, and T. C. Bond (2020), A Mineralogy-Based  
459 Anthropogenic Combustion - Iron Emission Inventory, *J. Geophys. Res.-Atmos.*, 125(17), e2019JD032114,  
460 doi:10.1029/2019jd032114.
- 461 Seo, H., and G. Kim (2023), Anthropogenic Iron Invasion into the Ocean: Results from the East Sea (Japan Sea), *Environ. Sci.*  
462 *Technol.*, 57(29), 10745-10753, doi:10.1021/acs.est.3c01084.
- 463 Shi, J., Y. Guan, A. Ito, H. Gao, X. Yao, A. R. Baker, and D. Zhang (2020), High Production of Soluble Iron Promoted by  
464 Aerosol Acidification in Fog, *Geophys. Res. Lett.*, 47(12), doi:10.1029/2019gl086124.
- 465 Shi, Z., M. D. Krom, T. D. Jickells, S. Bonneville, K. S. Carslaw, N. Mihalopoulos, A. R. Baker, and L. G. Benning (2012),  
466 Impacts on iron solubility in the mineral dust by processes in the source region and the atmosphere: A review, *Aeolian*  
467 *Res.*, 5, 21-42, doi:<https://doi.org/10.1016/j.aeolia.2012.03.001>.
- 468 Solmon, F., P. Y. Chuang, N. Meskhidze, and Y. Chen (2009), Acidic processing of mineral dust iron by anthropogenic  
469 compounds over the north Pacific Ocean, *J. Geophys. Res.-Atmos.*, 114(D2), doi:<https://doi.org/10.1029/2008JD010417>.
- 470 Tagliabue, A., A. R. Bowie, P. W. Boyd, K. N. Buck, K. S. Johnson, and M. A. Saito (2017), The integral role of iron in ocean  
471 biogeochemistry, *Nature*, 543(7643), 51-59, doi:10.1038/nature21058.
- 472 Wang, R., Y. Balkanski, O. Boucher, L. Bopp, A. Chappell, P. Ciais, D. Hauglustaine, J. Peñuelas, and S. Tao (2015), Sources,  
473 transport and deposition of iron in the global atmosphere, *Atmos. Chem. Phys.*, 15(11), 6247-6270, doi:10.5194/acp-15-  
474 6247-2015.
- 475 Westberry, T. K., M. J. Behrenfeld, Y. R. Shi, H. Yu, L. A. Remer, and H. Bian (2023), Atmospheric nourishment of global  
476 ocean ecosystems, 380(6644), 515-519, doi:10.1126/science.abq5252.
- 477 Zhang, H., et al. (2022), Abundance and Fractional Solubility of Aerosol Iron During Winter at a Coastal City in Northern  
478 China: Similarities and Contrasts Between Fine and Coarse Particles, *J. Geophys. Res.-Atmos.*, 127(1), e2021JD036070,  
479 doi:<https://doi.org/10.1029/2021JD036070>.
- 480 Zhu, Y., et al. (2022), Sources and processes of iron aerosols in a megacity in Eastern China, *Atmos. Chem. Phys.*, 22(4), 2191-  
481 2202, doi:10.5194/acp-22-2191-2022.

482